Journal of Applied Mechanics and Technical Physics, Vol. 38, No. 1, 1997

SPATIAL SUPERSONIC FLOWS AT TSTO SEPARATION OF AEROSPACE SYSTEMS

T. Bonnefond,[1] N. P. Adamov,[2] M. D. Brodetskii,[2] L. G. Vasenev,[2] E. K. Derunov,[2] and A. M. Kharitonov[2]

UDC 519.6+533.6.07

One of the most advanced concepts of future space reusable transportation systems are two-stage vehicles whose second stage is the orbital stage. Such concepts are used in the well-known Radiance (France), Sanger (Germany), and Boeing (USA) projects, as well as some others. When the first stage is equipped with an air-breathing engine, the stages are separated for Mach numbers $M_\infty = 6$–12 at altitudes of about 30 km and, hence, at high dynamic pressures. Under these conditions, the aerodynamic interference between the stages can exert a significant effect on the safety of the separation maneuver. In the general case, supersonic flow past separating vehicles is a complex three-dimensional gas-dynamic problem. An adequate numerical simulation of such flows requires a sophisticated understanding of the physical picture of interaction of the stages. This information can be a obtained from a complete aerophysical experiment that gives both total and distributed flow characteristics over wide ranges of flow parameters and relative positions of models. Decker and Gera [1] analyzed the total aerodynamic characteristics of a two-stage model for $M_\infty = 3$ and 6 for the purpose of computing the trajectories of the separating stages. Bernot [2] reported the results for the separation of the shuttle orbital stage model from the fuel tank for $M_\infty = 10$. The characteristics of specific configurations of separate vehicles are presented in [1, 2].

Brodetskii et al. [3, 4] analyzed detail pressure fields and reported a vast range of material for testing the numerical methods being developed for the calculation of two isolated bodies of revolution or for the interference of these bodies with a flat plate. The results of [3, 4] broaden our knowledge of this class of complex flows, but they are insufficient to develop adequate computational algorithms for separating winged configurations.

Numerical simulation of flow past aerospace systems in the process of separation of the stages was performed in [5–8]. Mukovozov [5] developed an empirical computational technique for computing the aerodynamic characteristics of the first stage (fuel tank) and of the orbital stage ("Buran" vehicle) under their separation. The results obtained are compared with experimental data in each particular case.

Numerical simulation of separation processes using two- and three-dimensional unsteady Euler and Navier–Stokes equations is described in [6–8]. Obviously, such numerical realizations require a careful verification by experimental data to determine regions of their applications.

In the present work, we used schematized models of the first and second stages to test experimentally models of the most promising TSTO concepts of two-stage systems. In such a setting, the experimental data obtained meet most fully the requirements of tests of the models developed and of the numerical-simulation methods for typical features of flow past stages under their separation. A detailed study of distributed characteristics in combination with visualization of the interfering shocks provides a more profound understanding of the conditions of formation of the interference components of aerodynamic forces and moments. Such information obtained for a wide range of flow parameters and relative positions of the first and second stages can be successfully used for the development of approximate methods for estimating the interference components.

---

[1]AEROSPATIALE, France. [2]Institute of Theoretical and Applied Mechanics, Siberian Division, Russian Academy of Sciences, Novosibirsk 630090. Translated from Prikladnaya Mekhanika i Tekhnicheskaya Fizika, Vol. 38, No. 1, pp. 21–29, January–February, 1997. Original article submitted October 30, 1995.

 0021-8944/97/3801-0018 $18.00 © 1997 Plenum Publishing Corporation

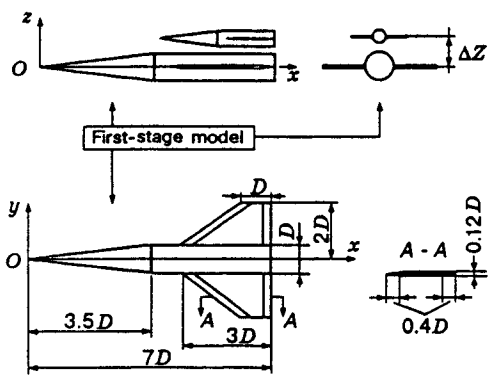

Fig. 1

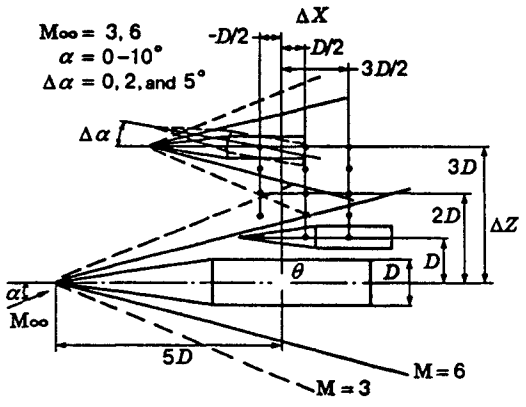

Fig. 2

Experimental Methods, Techniques, and Conditions. The first- and second-stage models are combinations of an axisymmetric conical–cylindrical body and a flat tapered wing with sharp leading and trailing edges (Fig. 1). The leading-edge sweep angle is $\Lambda = 53°$. The wing has a hexagonal profile with a constant spanwise thickness equal to 4% of the airborne chord. The wing is mounted on the airframe according to the mid-wing monoplane lay-out so that its trailing edge is located in the airframe base plane.

Model No. 1 is manufactured in two versions: one for measuring the aerodynamic forces and moments (balance version) and the other (pressure version) with provision for pressure measurements at twenty points on the generatrix of the airframe cylindrical part located in the vertical symmetry plane of the second-stage side.

The wing of model No. 1 is detachable. When special inserts are mounted in place of the wing, model No. 1 is converted into an isolated conical–cylindrical airframe (model No. 0 of the first stage), which was also used for balance or pressure tests.

The second-stage model is a half-sized copy of model No. 1 and is also manufactured in two versions (balance and pressure versions, Fig. 1). The pressure version allows for pressure measurements at seventeen points on the surface, five of which are located on the conical nose part. All pressure taps are located in the vertical symmetry plane of the model on the first-stage side.

By means of the tail sting with a shield, model No. 1 was mounted in an arc-shaped suspension of the standard mechanical balance of the wind tunnel. The balance α-mechanism ensured the range of angles of attack $\alpha = -4$ to 22°. The second-stage model was mounted on the holder of a specially developed benchmark. The benchmark ensured a simultaneous change in the angles of attack of the second- and first-stage models within the range $\alpha = 0$–10°. At the same time, the benchmark made it possible to simulate the separation of the second stage from the first stage for the following ranges of linear and angular quantities:

— discrete displacement[1] of the second stage in the transverse direction, $\Delta Z = D$–$3D$ (50–150 mm);

— longitudinal displacement[1] of the second stage relative to the first stage, $\Delta X = -0.5D$–$1.5D$ (0–100 mm) performed using the remote control panel of the holder displacement mechanism;

— angular deflection of the second-stage model relative to the first-stage model for angles of attack $\Delta\alpha = 0$, 2, and 5° (performed discretely by rotating the holder relative to the center of mass of the second stage).

The experiments were performed in a T-313 supersonic wind tunnel [9] at the Institute of Theoretical and Applied Mechanics, Siberian Division, Russian Academy of Sciences for Mach numbers $M_\infty = 3.01$ and 6.11 and Reynolds numbers $Re_1 = (9 \text{ and } 35) \cdot 10^6$ m^{-1}, and $18 \cdot 10^6$ m^{-1}. During the experiments, the parameters of the relative model positions ΔZ, ΔX, and $\Delta\alpha$ (Fig. 2) were varied, and the angles of attack

[1]The relative position (distances ΔZ, ΔX) of the first- and second-stage models are found using the conditional centers of mass located on the longitudinal axis of the model at a distance of two diameters from the base plane.

TABLE 1

ΔC_A	ΔC_N	ΔC_m	ΔC_p
First stage			
±0.01	±0.02	±0.02	±0.015
Second stage			
±0.015	±0.03	±0.03	±0.02

were within $\alpha = 0$–$10°$ with an increment of 2°.

The aerodynamic forces and moments of the first-stage model were measured by the standard AV-313M mechanical balance of the wind tunnel, and those of the second-stage model were measured by a strain-gage balance designed for the following limiting loads: longitudinal force $R_x = 15$ kg, normal force $R_y = 15$ kg, and pitching moment $M = \pm 0.5$ kg · m. The pressure distributions on the models of both stages were measured by an MID-100 multichannel pressure gage [10] with an accuracy of 0.3.

The results were processed using special codes. The processing for each stage included calculations of the coefficients of the longitudinal force $C_A = -R_x/qS$, of the normal force $C_N = -R_y/qS$, and of the pitching moment $C_m = M/qSL$ in the fixed right-hand coordinate system whose origin for each stage coincided with the model tip (see Fig. 1). The mid-section area was used as the reference area S, and the length of the corresponding stage was used as the reference length L. The pressure coefficients $C_{p_i} = (p_i - p_\infty)/q$ were calculated in the processing of the pressure tests.

The results of the metrological tests confirmed fairly low random errors and good agreement of the characteristics obtained at different times. At the same time, they revealed some other factors that increase the error of the aerodynamic coefficients: velocity-field nonuniformity, errors of mounting the models in the required position, errors of determining the corrections for the base pressure, temperature effect on the strain-gage balance indications.

These errors are classed among systematic errors, but because of their small values and for some other reasons, they cannot be taken into account in experimental-data processing. Hence, they increase the total error of the results obtained. With allowance for this circumstance, the analysis of the results obtained provides the following estimates of the maximum total errors of aerodynamic coefficients for $M_\infty = 3$ (see Table 1).

Pressure Distribution. Detailed investigation of the pressure distribution combined with flow visualization gives a more comprehensive idea of the conditions of formation of interference loads during the stage separation process. In particular, Fig. 3 shows the distribution of the pressure-coefficient increments ΔC_{p_i} along the first-stage model without wings (model No. 0) at $\Delta\alpha = 0$ and 5°, $\alpha = 6°$, $\Delta X = 0.5D$, and $\Delta Z = D$ and $1.5D$. As the increments we used the differences between the measured pressure coefficients C_{p_i} and the corresponding reference values obtained for $\Delta Z/D = \infty$, i.e., $\Delta C_p = C_p - C_{p_{ref}}$. Examination of the graphs of $\Delta C_{p_i}(\bar{x})$ ($\bar{x} = x/L$) for $\Delta Z/D = 1.0$, 1.5, 2.0, 2.5, and 3.0 shows that the interference region for the first-stage model is restricted to the interval $\Delta Z/D < 2.5$. For $\Delta Z = D$, the positive coefficients ΔC_p on the upper generatrix are an evident consequence of the increase in the bow shock wave of the second stage and in the conical flow field behind the shock wave. Behind the shock wave, ΔC_p increases suddenly to a maximum value (region I), and, downstream, it decreases to zero and further takes negative values (region II). The latter is caused by the expansion fans from the second and first (reflected fan) stages. The doubly reflected bow shock wave from the second stage for $\Delta Z = D$ is responsible for the second positive pressure region in the rear part of the body (region III). Note also that for $\Delta\alpha = 5°$, the maximum values of ΔC_p exceed those at the zero relative angle of the second stage for angles of attack $\alpha = 0$ and $\alpha = 6°$ (Fig. 3).

Thus, for the range of governing parameters studied, the effect of the second stage on the first stage at $\Delta Z/D < 2.5$ reduces primarily to the formation of one or two elevated pressure regions on the lee surface, which reduce the lift force of the first stage and the absolute value of the pitching moment. This is also

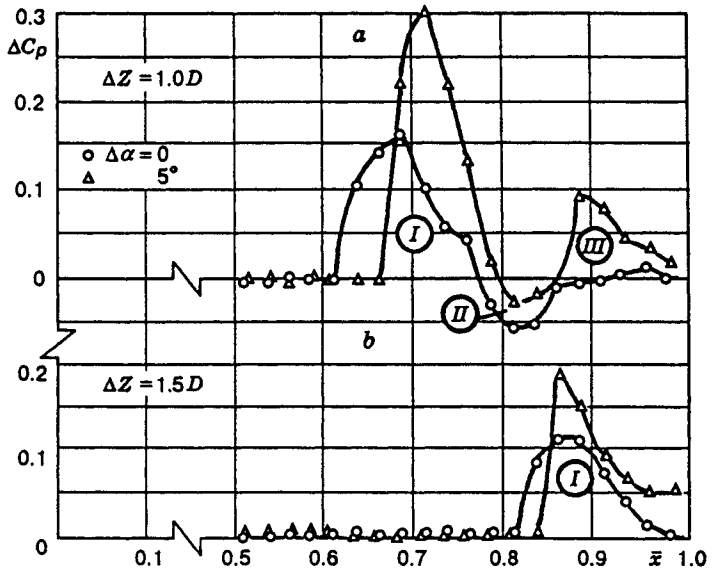

Fig. 3

confirmed by the results given in Fig. 4, which shows a schlieren picture of visualization of the flow pattern between the models and the distributions of the pressure coefficients on the first and second stages for $\Delta Z = D$ and $\alpha = 6°$. The scale of the graphs of $\Delta C_p(\bar{x})$ in the x direction is the same as the scale of the photographs. In this position ($\Delta X = 0.5D$), the second-stage model is almost entirely located within the conical flow region behind the first-stage bow shock wave. For $\Delta Z = D$, as is evident from Fig. 4, two regions of positive interference and two regions of negative interference are formed along the generatrix of the second-stage model. The first region is caused by the arrival of the first-stage bow shock wave at the nose part of the second-stage model.

Region II results from the effect of the expansion fan of the first-stage model, and region III is caused by the incidence of the second-stage bow shock reflected from the first stage and by the shock wave from the first-stage wing that practically coincides with the former shock wave. Finally, region IV is caused by the second-stage expansion fan reflected from the first stage and by the expansion fan from the crancked leading-edge wing of the first-stage. Note that the wing of model No. 1 in this position has little or no effect (Fig. 4). In the general case, the number of interference regions and the relations among them are substantially dependent on the distances ΔZ and ΔX and on the angle of attack α and, for small ΔZ, on $\Delta\alpha$, in addition.

Thus, the formation of interference loads is caused by the interaction of shocks and expansion waves with one another and with the boundary layers developed on the model surfaces.

Formation of Interference Loads. Analysis of a great number of experimental curves of the interference components of the coefficients of the forces and of the pitching moment versus the relative-position parameters of the models confirms that, for the second-stage model, these curves have a much more complicated character than for the first stage. Therefore, below, we consider specific features of variation in the aerodynamic-coefficient increments for the second stage under its interaction with model No. 1 with respect to the corresponding values obtained for $\Delta Z = \infty$. We confine ourselves to the characteristics of the normal force ΔC_N, since the variation in the pitching moment is primarily determined by the character and magnitude of this force.

As an illustration, Fig. 5 shows the ΔC_N increments for the second-stage model as a function of α and ΔZ for $\Delta X = -0.5D$, $0.5D$, and $1.5D$. As the second-stage model is displaced from the fore position $\Delta X = -0.5D$ to the rear position $\Delta X = 1.5D$, the distance ΔZ between the stages being varied from D to $3D$, various factors are realized that determine sequentially (in some cases, simultaneously) the character and values of the interference loads. Some of these factors increase the lift force (positive interference), and others decrease it (negative interference). Among the first are: (1) arrival of the bow shock wave from the first stage

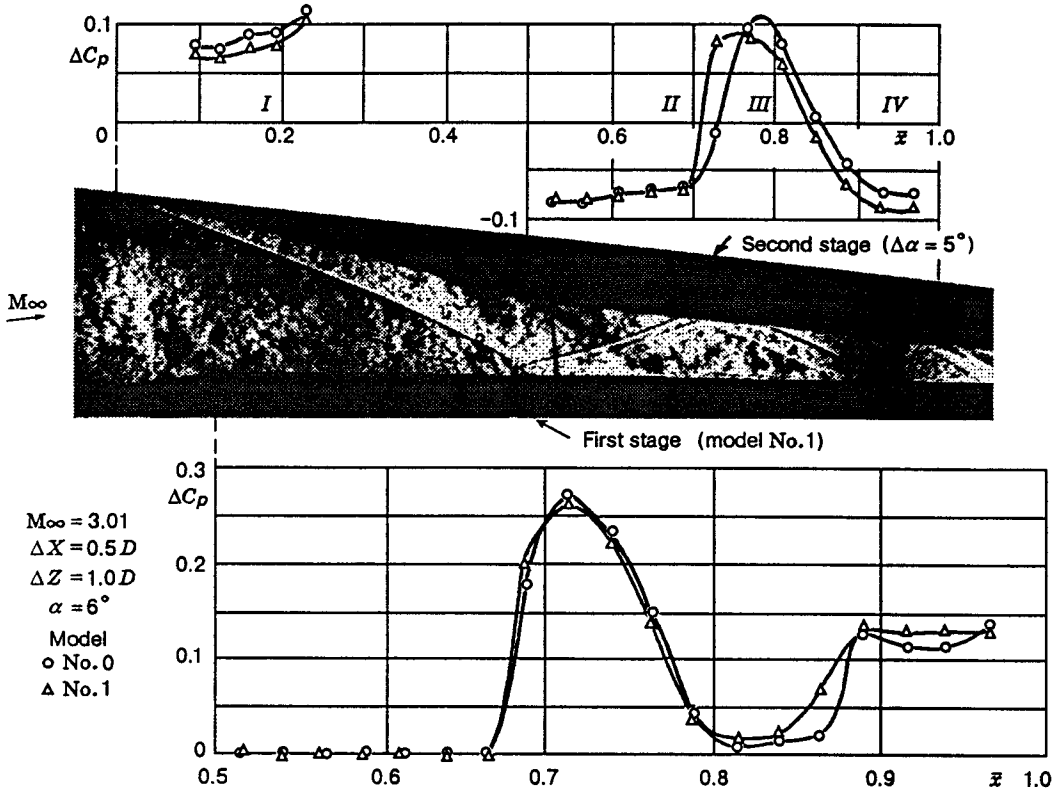

Fig. 4

on the windward side of the second stage, (2) positive flow downwash in the conical flow field behind the bow shock wave from the first stage, (3) arrival of the doubly reflected bow shock from the first stage, (4) reflected bow shock from the second stage; the second group of factors include: (5) the influence of the expansion fan from the first stage, (6) the expansion fan reflected from the second stage, and the factors related to the varied angle of attack, namely: (7) a decrease in the first-stage bow shock intensity on the lee side, (8) a decrease in the flow downwash on the lee side of the conical flow field of the first stage, (9) the flow turning toward the first-stage upper surface behind the expansion fan for small ΔZ, which decreases the positive downwash of the flow past the lower surface of the second stage.

Depending on the relative position of the stages, various combinations of these factors affect the formation of interference loads. In particular, Fig. 5a shows that for $\Delta X = -0.5D$, the effect of the first stage is observed even for $\Delta Z = 2.5D$ and $\alpha > 6°$, when the bow shock wave is incident on the rear part of the second stage. As the distance between the models becomes shorter, the bow shock wave from the first stage is shifted forward along the second-stage body. As a result, for $\Delta Z = 2D$ and $\alpha = 0$, an additional moderate force $C_{N_0} \approx 0.05$ appears, which grows with an increase in α to 5°. With a further increase in α, the increase in the normal force is compensated for by the reduction in the intensity of the bow shock wave from the lee side (factor 7). Therefore, the value of ΔC_N remains practically constant within the interval $\alpha = 5$–$10°$. For $\Delta Z = 1.5D$ and $\alpha = 0$, the bow shock wave from the first stage is incident on the forebody of the second stage, and a great part of its surface is in the conical flow region.

An additional positive flow downwash behind the bow shock (factor 2) is responsible for an increase in the normal force and drag. However, with the increase in α due to the effect of factor 7 and a decrease in the flow downwash on the lee side of the conical flow (factor 8), the positive interference decreases monotonically. At the minimum distance $\Delta Z = D$ and $\alpha = 0$, the first-stage bow shock is shifted to the second-stage tip. In this case, in addition to factors 1 and 2, the value of ΔC_{N_0} is affected by the doubly reflected bow shock wave and expansion fan from the first stage (factors 3 and 5) and also by the reflected bow shock and expansion

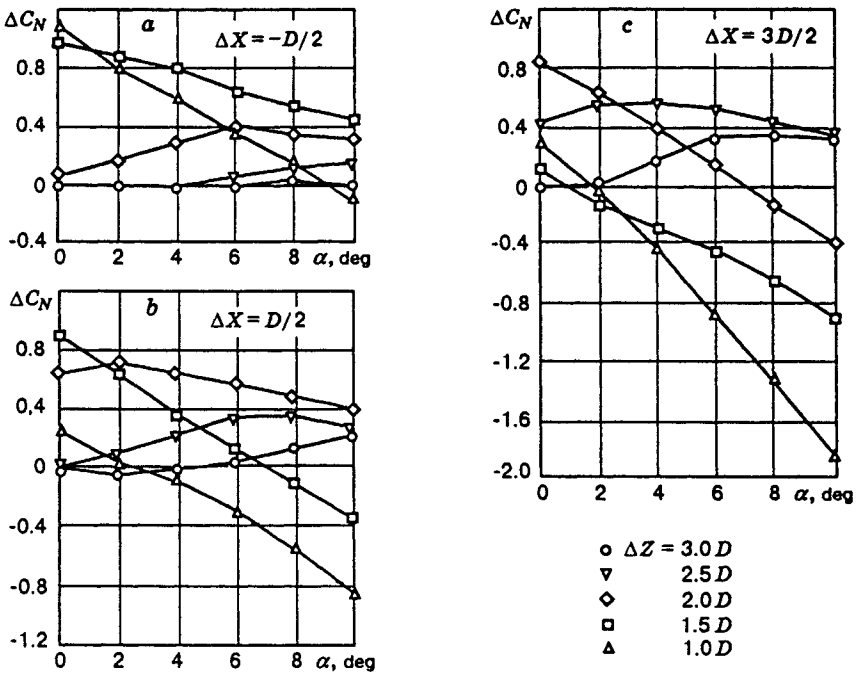

Fig. 5

fan from the second stage (factors 4 and 6). As a result, ΔC_{N_0} somewhat increases and acquires the highest value over the entire interaction region (30% of the maximum normal force of the isolated second stage at $\alpha = 10°$). With the increase in α, the combined effect of factors 5–9 decreases the downwash angle of the flow past the lower surface of the second stage and, hence, decreases monotonically the lift force. As a result, a linear decrease in the positive interference takes place. At the same time, the second-stage drag considerably increases for $\alpha = 0$ and decreases with an increase in α.

When the second stage is positioned at $\Delta X = 0.5D$ (Fig. 5b), the effect of the first stage is observed even for $\Delta Z = 2.5D$, $\alpha \geqslant 0$ and $\Delta Z = 3D$, $\alpha \geqslant 6°$, i.e., at a greater distance from the first stage than for $\Delta X = -0.5D$. In this case, the character of the ΔC_N variation versus the angle of attack and the values of ΔC_N are similar to those in the case of $\Delta X = -0.5D$. As the second stage approaches the first stage, the above factors are in sequence responsible for changes in the normal force. However, because of the more backward position of the bow shock incidence for $\Delta Z = 2D$, the values of ΔC_N within $\alpha = 0$–$6°$ are smaller than in a similar situation for $\Delta X = -0.5D$ and $\Delta Z = 1.5D$. For $\Delta Z = 1.5D$, the formation of the interference load is also influenced by the above factors, except for factors 3, 4, and 6. As a result, the increment ΔC_{N_0} acquires a maximum value in this position. At the same time, with the increase in α, factors 5 and 7–9 begin to play a determining role, and ΔC_N decreases linearly and changes its sign at $\alpha = 7°$. In the closest position ($\Delta Z = D$), the second stage is located behind the bow shock from the first stage. In this case, only a certain portion of its cone is located in the conical flow field, while the major portion of its lifting surface is located downstream of the characteristic cone of the expansion fan, i.e., in a weakly disturbed flow. Factor 2 is of lesser importance here, while a significant effect is exerted by factors 4–6 and, probably to a lesser extent, by the reflected shock wave from the second-stage wing. Hence, for a considerably smaller value of ΔC_{N_0} with an increase in α, the positive interference vanishes even at $\alpha = 2°$ and the negative interference increases linearly, decreasing thereby the lift force of the second stage. The second-stage drag decreases noticeably as well.

In the very backward position $\Delta X = 1.5D$ (Fig. 5c), the first-stage effect is observed even for $\Delta Z = 3D$ and $\alpha \geqslant 2°$. In this case, the curve of $\Delta C_N(\alpha)$ is qualitatively and quantitatively similar to that for $\Delta X = 0.5D$, $\Delta Z = 2D$ and $2.5D$. For $\Delta Z = 1.5D$, the second stage enters the flow region directed along the

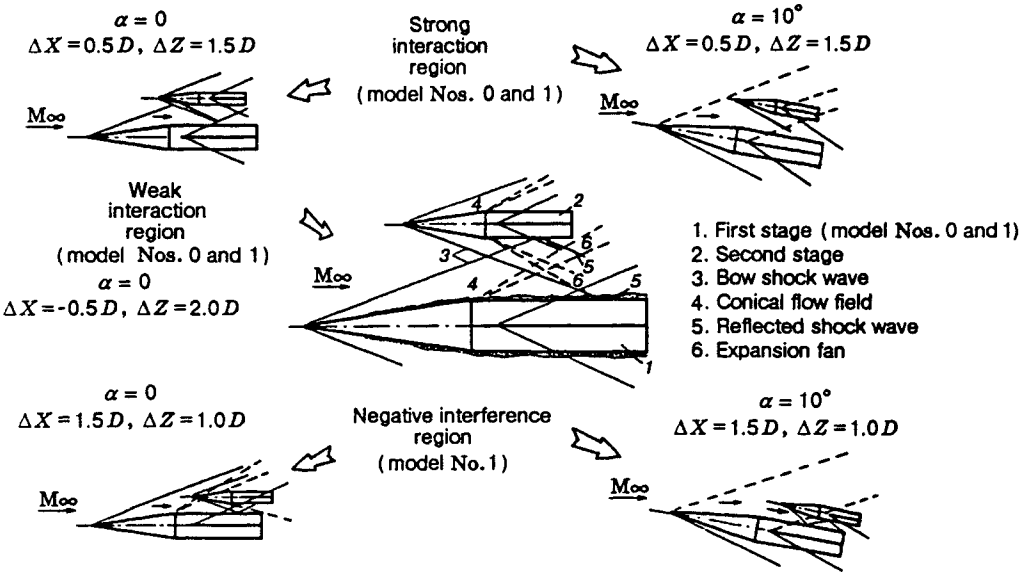

Fig. 6

first-stage upper surface (factor 9). In this case, the downwash of the flow past the second-stage lower surface decreases, and this decreases considerably its lift force with an increase in α. This region is characterized by negative interference. As the stages approach each other ($\Delta Z = D$), the second stage nearly leaves the characteristic cone of the first stage, and, for $\alpha = 0$, factors 4 and 6 seem to compensate each other. With an increase in α, the flow turning exerts a determining effect (factor 9). As a result, the negative value of the interference component ΔC_N increases considerably (almost linearly), and, at $\alpha = 10°$, it reaches 60% of the corresponding value for the isolated second stage. In this case, the vortex structures on the lee side of the first-stage body have an additional effect on the negative interference. A noticeable reduction in the longitudinal force coefficient is also observed.

In the interaction of the second stage with model No. 0 (a body without wings), the difference in the increments ΔC_N manifests itself only for $\Delta Z = D$ in the decreased negative interference in the middle and backward positions of the second-stage model ($\Delta X \geqslant 0.5D$ and $\Delta Z \leqslant 1.5D$) with an increase in α. When the second stage is placed at a relative angle $\Delta\alpha = 5°$, the effect of factors 1, 2, and 4 is more pronounced, but, at the same time, the negative role of factor 8 increases at angles of attack. As a result, in the interaction with model Nos. 0 and 1, the behavior of the interference components of the normal forces and the values of these components are similar.

Thus, the resultant values of interference loads are determined by the effect of some combination of the above factors. A detailed analysis of the measured total aerodynamic characteristics combined with the schlieren pictures of the flow allows one to identify three typical interference regions (Fig. 6).

A weak interference region forms when the bow shock from the first stage strikes the rear part of the second stage (i.e., the rear part of the model is displaced along the shock), and the formation of the interference components is mainly determined by factors 1 and 7.

A strong interference region forms when a considerable portion of the second-stage lifting surface is located in the conical flow between the bow shock wave from the first stage and its expansion fan. This region is characterized by a substantial growth in the positive interference ΔC_{N_0} at zero angles of attack and by a substantial negative gradient of $\Delta C_N(\alpha)$.

A negative interference region forms for small values of ΔZ in backward positions of the second stage, in which the flow turning between the models toward the first-stage upper surface up to the trailing-edge shock wave and vortex structure on the lee side of the body plays an important role at angles of attack. In this case, the lift force of the second stage decreases considerably.

REFERENCES

1. J. P. Decker and J. Gera, "An exploratory study of parallel-stage separation of reusable launch vehicles," NASA TND-4765 (1968).
2. P. T. Bernot, "About separation study of a shuttle orbiter and external tank at hypersonic speeds," NASA-TMX-3212 (1975).
3. M. D. Brodetskii and E. K. Derunov, "Aerodynamic interference of two bodies of revolution at supersonic speeds," in: *Interference of Complex Spatial Flows* [in Russian], Inst. of Theor. and Appl. Mech., Sib. Div., Acad. of Sci. of the USSR, Novosibirsk (1987), pp. 39–53.
4. M. D. Brodetskii, E. K. Derunov, A. V. Zabrodin, and A. E. Lutskii, "Comparison of numerical and experimental results of supersonic flow around a combination of two bodies of revolution," *Teplofiz. Aeromekh.*, **2**, No. 2, 97–102 (1995).
5. M. V. Mukovozov, "A method for determining interference components of aerodynamic characteristics of aircraft integrated with a body of revolution at Mach 3–6," in: *Applied Problems of Aeromechanics and Geo-Cosmic Physics* [in Russian], Phys.-Tech. Inst., Moscow (1990).
6. P. Brenner, "Numerical simulation of three-dimensional and unsteady aerodynamics about bodies in relative motion applied to a TSTO separation," AIAA Paper No. 93-5142, New York (1993).
7. W. Schroder and G. Hartmaun, "Analysis of inviscid and viscous hypersonic flows past a two-stage spacecraft," *J. Spacecraft Rocket*, **30**, No. 1, 8–13 (1993).
8. W. Schroder, R. Behr, and S. Menne, "Analysis of hypersonic flows around space transportation systems via CFD methods," AIAA Paper No. 93-5067, New York (1993).
9. I. I. Volonikhin, V. D. Grigor'ev, V. S. Dem'yanenko, et al., "A T-313 supersonic wind tunnel," in: *Aerophysical Research* [in Russian], Inst. of Theor. and Appl. Mech., Sib. Div., Acad. of Sci. of the USSR, Novosibirsk (1972).
10. M. D. Brodetskii, Yu. I. Vyshenkov, A. M. Kharitonov, et al., "A MID-100 multichannel pressure transducer," in: A. M. Kharitonov (ed.), *Methods and Techniques of Aerodynamic Research* [in Russian], Inst. of Theor. and Appl. Mech., Sib. Div., Acad. of Sci. of the USSR (1978).